

Electrons Generate Self-Complementary Broadband Vortex Light Beams Using Chiral Photon Sieves

Nika van Nielsen, Mario Hentschel, Nick Schilder, Harald Giessen, Albert Polman, and Nahid Talebi*

Cite This: *Nano Lett.* 2020, 20, 5975–5981

Read Online

ACCESS |

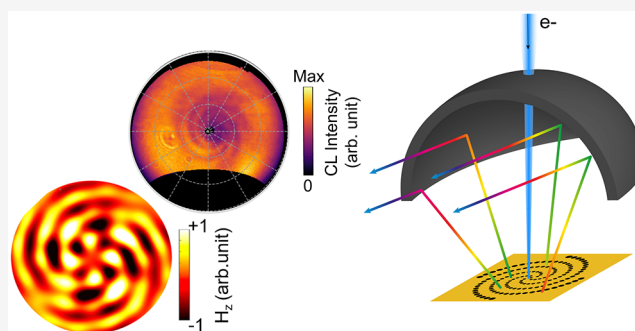
Metrics & More

Article Recommendations

Supporting Information

ABSTRACT: Planar electron-driven photon sources have been recently proposed as miniaturized light sources, with prospects for ultrafast conjugate electron–photon microscopy and spectral interferometry. Such sources usually follow the symmetry of the electron-induced polarization: transition-radiation-based sources, for example, only generate p-polarized light. Here we demonstrate that the polarization, the bandwidth, and the directionality of photons can be tailored by utilizing photon-sieve-based structures. We design, fabricate, and characterize self-complementary chiral structures made of holes in an Au film and generate light vortex beams with specified angular momentum orders. The incoming electron interacting with the structure generates chiral surface plasmon polaritons on the structured Au surface that scatter into the far field. The outcoupled radiation interferes with transition radiation creating TE- and TM-polarized Laguerre–Gauss light beams with a chiral intensity distribution. The generated vortex light and its unique spatiotemporal features can form the basis for the generation of structured-light electron-driven photon sources.

KEYWORDS: Electron-driven photon source, chiral, angular momentum, cathodoluminescence angle-resolved mapping, plasmon polaritons, chain plasmons



INTRODUCTION

Electron beams interacting with materials and nanostructures can cause electromagnetic radiation, with various mechanisms involved,¹ such as transition and diffraction radiation,² Cherenkov radiation,³ and Bremsstrahlung.⁴ Electron-driven radiation has been mostly utilized as diagnostic schemes or characterization techniques; namely, through detecting high-energy charged particles, as for Cherenkov radiation,⁵ mapping quasiparticle excitations such as plasmons and excitons,⁶ and elemental mapping of atomic structures by characteristic X-rays.⁷ Additionally, in 1953, Smith and Purcell proposed the interaction of electrons with optical gratings for the generation of coherent light waves.⁸ The so-called Smith–Purcell radiation occurs due to synchronicity between the traveling time of electrons and photons alongside the grating axis enabled by the smaller phase velocity of higher-order optical Floquet modes of the grating. Smith–Purcell radiation is routinely used to generate THz radiation in so-called Orotion sources.⁹

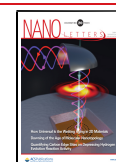
Recently, the demand for the generation of planar few-photon coherent sources with tailored properties has raised interests toward metamaterial-based¹⁰ and holographic free-electron-driven photon sources.¹¹ Particularly, it was shown that such sources have promising applications in correlated electron-photon spectroscopy and ultrafast microscopy with electron microscopes.¹² Specifically, for applications in ultrafast microscopy, we have recently designed and characterized a broadband

electron-driven photon source, based on a photon sieve structure.¹³ This structure is composed of an array of nanoholes incorporated into a thin gold film, distributed in such a way to manifest an adiabatic increase in the periodicity of the lattice; hence, generating Gaussian-beam-like focused radiation upon electron beam irradiation. Here, we demonstrate that a chiral pattern of nanoholes can be used to generate Laguerre–Gaussian-like beams and that they can achieve vortex light sources with precise control over the pattern of phase singularities and the orbital angular momentum of light. Light and matter waves with a twist have various applications in quantum optics, investigating the selection rules and coherent control.^{14–22} Vortex light and vortex plasmons can be generated as a result of the interaction of emitters and far-field light with chiral patterns like Archimedes spiral patterns.^{23,24} Thus, merging twisted light with electron-driven photon sources paves the way toward correlative electron-photon spectroscopy with twisted light.

Received: May 7, 2020

Revised: July 8, 2020

Published: July 9, 2020



Cathodoluminescence (CL) angle-resolved mapping is used to characterize the electron-induced radiation from our structures. We show that the generated vortex light is broadband, covering the entire visible-to-near-infrared spectral range. Our CL experimental results show good agreement with finite-difference time-domain (FDTD) simulations. Indeed creating vortex light using Archimedes spiral patterns interacting with electrons has been already proposed.²⁵ Here, unraveling the dynamics of the interaction using our FDTD simulations, we highlight the screwing principle of the generated vortex light, the morphology of the phase singularity regions, as well as the emergence of both TE- and TM-polarized Laguerre–Gaussian vortex beams. Moreover, we observe ultrabroadband vortex light covering the wavelengths of 380 to 900 nm. Particularly, the latter are formed due to the self-complementary nature of our structural design in such a way that both surface and void plasmons propagate along and in between the chiral arms, respectively. We thus achieve a design principle for structured-light generation, and in particular, generation of vortex light with broadband and hybrid nature suitable for coherent control of nanophotonic systems in an electron microscope.

RESULTS AND DISCUSSION

Design Principle. Planar chiral arms composed of holes in a metal film are generated using a generic mathematical description given by

$$(x_i, y_i) = 2 \times 10^{-6} t (\cos(2m\pi t + \varphi_i), \sin(2m\pi t + \varphi_i)) \quad (1)$$

where t is a control parameter defined on the interval $t \in [0, 1]$. Here, (x_i, y_i) define the coordinates of the holes with respect to the origin. More specifically, the parameter t is discretized as $t_n = (n\gamma)^\alpha$ with n being an integer $n = 0, 1, \dots, N$ and $\alpha < 1$ and $\gamma < 1$ are parameters used to enable inhomogeneous discretization controlling the distance between nanoholes in the arms. Also the radius of each hole is given by $R_n = (R_i + t_n^2 \times R_s)$, where $R_i = 50$ nm and $R_s = 150$ nm. The radii of the holes are therefore adiabatically increased from 50 nm at the origin to 200 nm at the outer rims along the spiral to achieve broadband emission and the center-to-center distance between the adjacent holes changes from 150 to 450 nm. Since the size of the holes specifies the resonant frequency of induced magnetic dipolar moments, the smooth change of the hole size helps to realize a broadband spectrum for the vortex light. m is the winding parameter and defines the interarm distance impacting the compactness of our structures. Its value for different structures is denoted later. The subscript i reflects the arm number, and the initial direction of each chiral arm at the origin is given by φ_i . The vortex number of the generated light in the far field is determined by the number of arms. Both clockwise ($m < 0$) and anticlockwise ($m > 0$) spirals were made, which generate clockwise and anticlockwise vortex beams propagating upward. Light with inverse winding number propagates downward from the structure.

We investigate three structures composed of two, three, and four chiral arms, attained by introducing $m = +2$ and $\varphi_i \in (0, \pi)$, $m = +1.5$ and $\varphi_i \in (0, 2\pi/3, 4\pi/3)$, and $m = +1$ and $\varphi_i \in (0, \pi/2, \pi, 3\pi/2)$ into eq 1. The m values are controlled to maintain the same interarm distance. These structures were fabricated by drilling nanoholes into a 40 nm thick evaporated gold film on top of a 20 nm thin Si_3N_4 membrane using focused-ion-beam milling. A void ring was fabricated around each structure, which

acts as mirror for propagating surface plasmon polaritons (SPPs) hence enhancing the efficiency of light generation from the nanoholes. Scanning electron microscopy (SEM) images of the three spiral geometries are shown in Figure 1a.

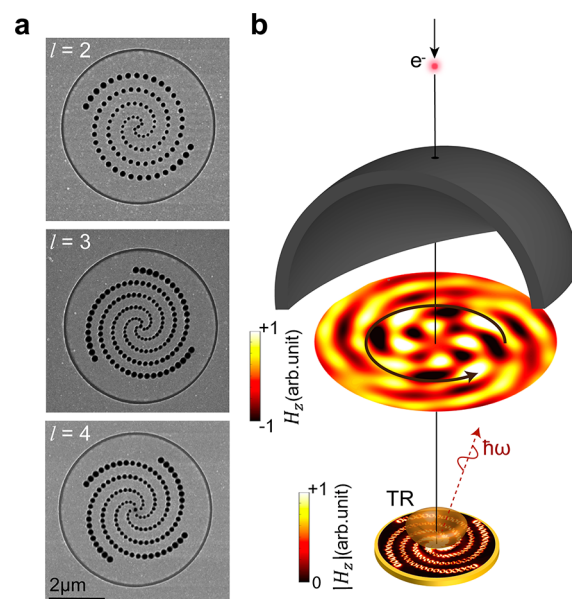


Figure 1. (a) SEM images of fabricated counterclockwise spiral structures with 2, 3, and 4 arms composed of chains of holes in a gold film. l indicates the total topological charge we expect to observe in the far field. (b) Schematic of interaction of the p-polarized evanescent field of a swift electron with a counterclockwise spiral structure. The electron simultaneously generates transition radiation and SPPs that partly scatter into magnetic localized surface plasmons of the holes propagating along the spiral chains. The outscattered light is composed of broadband right-handed fields with orbital angular momentum (vortex light) in both the near- and the far-field zones. The bottom image shows the magnitude of the z-component of the magnetic field at 5 nm above the surface. The center image shows the amplitude of the magnetic field component at 500 nm above the structure. The parabolic mirror that collects the CL is also indicated.

Nanoholes in a noble metal film can host resonant plasmonic magnetic dipole moments, according to Babinet's principle, analogous to the excitation of electric dipoles in a metal nanoparticle.^{26–29} Radially propagating SPPs excited on the surfaces of the gold film interact with the holes and cause the excitation of the magnetic dipole inside the nanoholes. For the thin gold film used here, both the quasi-symmetric and quasi-antisymmetric SPP charge distributions are excited with the quasi-symmetric SPP distribution decaying more slowly (see [supplementary Figure S3](#)). The symmetry is determined by the induced charge densities at the upper and lower surfaces. The induced magnetic dipole in each hole couples to the magnetic dipoles in adjacent holes, resulting in the propagation of energy via radiative energy exchange, akin to the dipolar interactions along a chain of nanoparticles, which are not positioned in the near-field regions of each other.^{30–32} Indeed, for most of the nanoholes, the distance between the adjacent holes is above 100 nm; therefore, near-field interaction is negligible. Propagating chain plasmons along chiral arms, in contrast to SPPs, can effectively couple to the far field creating the vortex light (Figure 1b).

Angle-Resolved Cathodoluminescence Distributions. To determine the characteristics of the generated vortex light,

we use angle-resolved cathodoluminescence spectroscopy with 30 keV electrons. The angle-resolved CL distributions are shown in Figure 2 for the three spiral structures, both at a single

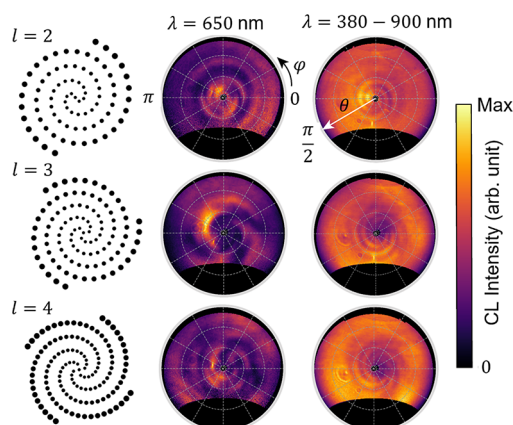


Figure 2. Angle-resolved CL distributions (30 keV) for counter-clockwise spiral structures that generate light with $l = 2, 3$, and 4 phase cycles, at 650 nm and over a 380 – 900 nm bandwidth.

wavelength of 650 nm (bandwidth 40 nm) and over the full bandwidth of the detector (380 – 900 nm). In all cases, the location of electron impact was chosen to be almost at the center of the structure. The angle-resolved maps show clear characteristic spiral features that are beamed upward from the sample. This contrasts with the common case of an electron beam exciting a planar metal film, for which transition radiation (TR) is observed with distinct high-angle lobes and little upward emission. The number of the winding arms matches with that of the fabricated structure, highlighting the relation between the number of the arms and the orbital angular momentum of the light. However, we observe that the handedness of the observed winding arms is opposite to the orientation of the arms of the fabricated structure. This can be explained as follows. As angular momentum results from the dynamics of fields that are evolving in time, its handedness is imprinted in the temporal evolution of the electromagnetic fields. However, we measure the time-

averaged intensity distribution in space. In this geometry, we generate both transition radiation originating from an electron beam traversing a multilayer system and vortex fields generated by scattering from nanoholes. Because their wavefronts have different radii of curvature (smaller for TR), it can be shown from eq 2 that this leads to effective inertia around the optical axis. This implies that at each instance in time, this results in curved arms with a handedness in space that is opposite to the temporal rotation direction (see Figure 1b and supplementary movie).

Optical waves with orbital angular momentum are generally represented by an expansion in the Laguerre–Gaussian (LG) orthonormal basis in cylindrical coordinates (ρ, θ, φ) , as

$$U_{pl}(\rho, \varphi, z) = \frac{A_{pl}}{W(z)} \left(\frac{\sqrt{2}\rho}{W(z)} \right)^{|l|} L_p^{|l|} \left(\frac{2\rho^2}{W^2(z)} \right) \exp \left(-\frac{\rho^2}{W^2(z)} \right) \times \exp \left(ik_0 z + \frac{ik_0 \rho^2}{2R(z)} + il\varphi - i\psi_G(z) \right) \quad (2)$$

where ρ and θ are the radius and azimuthal angle respectively, z is the axis of propagation, A_{pl} is a normalization constant, $W(z) = W_0 \sqrt{1 + (z/z_R)^2}$, $z_R = \frac{1}{2} k_0 W_0^2$ is the Rayleigh range, k_0 is the free-space wavenumber, $R(z) = z(1 + (z_R^2/z^2))$, and $\psi_G = (2p + |l| + 1) \tan^{-1}(z/z_R)$ is the Gouy phase. $L_p^{|l|}$ is the Laguerre polynomial, with l being the angular momentum order and p the order of radial variations. The time-averaged angular momentum density of the LG waves along the z -axis is given by $M = (l/\omega)|U_{pl}|^2$.²⁰ LG waves are solutions to the paraxial wave equation. Interestingly, our electron-driven photon sources demonstrate such beaming characteristics as well (see supplementary Figure S1, for 3D field distribution).¹³ Here, we demonstrate a qualitative comparison between the generated optical waves from our source and LG waves. The scalar wave function $U_{pl}(\rho, \varphi, z)$ in eq 2 is related to either the z -component of the electric field, or to the z -component of the magnetic field, depending whether TM or TE polarizations are considered, respectively. An electron beam traversing a thin metallic film generates TR with a nonzero z -component of the electric field,

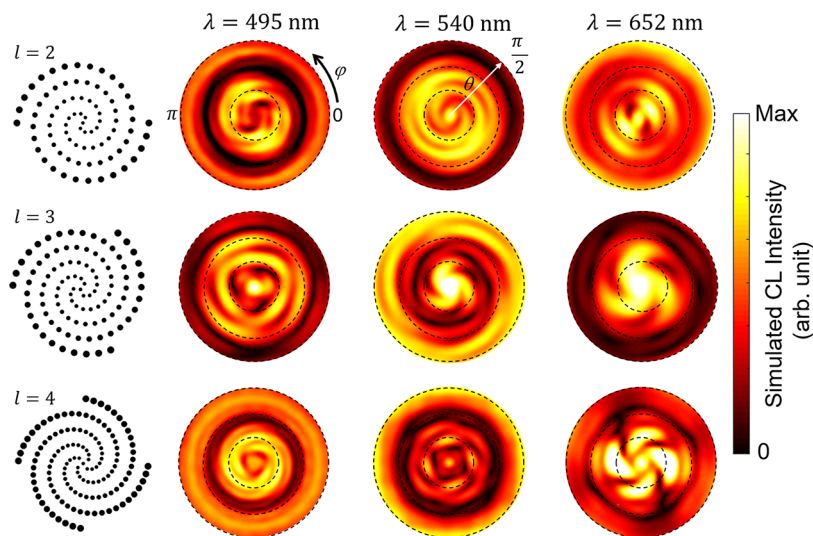


Figure 3. Simulated angle-resolved CL distributions in the far field for counter-clockwise spiral structures that generate light with $l = 2, l = 3$, and $l = 4$, at depicted wavelengths for a 30 keV electron incident at the center of the spiral.

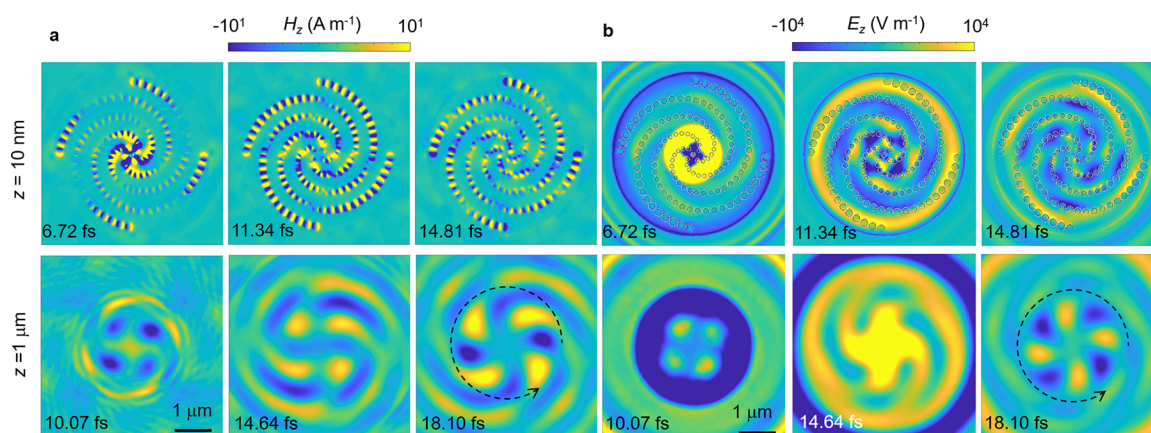


Figure 4. Snapshots of the spatial distribution of time-dependent z -component of the magnetic (a) and electric (b) fields at depicted times, in the near field zone $z = 10$ nm above the surface (top row) and in the far field zone $z = 1 \mu\text{m}$ above the surface (bottom row), for the counterclockwise spiral structure with 4 chiral arms. The electron reaches the upper surface of the gold film at $t = 0$ fs. Radially propagating electron-induced excitation leads to SPPs scattering off the holes and propagating at the areas between the chains, generating magnetic chain plasmons along each spiral. The coherent superposition of all scattered waves leads to right-handed Laguerre–Gaussian TM_z - and TE_z -polarized optical waves in the far field. Dashed circular arrows demonstrate the twisting direction of the generated vortex beams.

but the z -component of the magnetic field remains zero. However, due to the excitation of magnetic dipole moments in the nanopinhole in our structured thin films, a z -component for the magnetic field will be generated as well. Thus, our structures lead to the generation of hybrid waves, which, for clarification, we describe as a superposition of TE and TM waves.

In LG beams the parameter l in eq 2 reflects the azimuthal phase variation of the field, and its value corresponds to the order of the phase singularity at the center of the beam. The field intensity sustains a typical donut-like shape for $p = 0$, whereas its radius depends on the value of l (see [supplementary Figure S2](#)). Therefore, given the fact that our CL apparatus detects the time-averaged intensity of the field, we would expect to observe such donut-like intensities, contrary to the observed winding arms. In more detail, our angle-resolved CL maps are theoretically described as $\Gamma^{\text{CL}}(\varphi, \theta; \omega) = (1/\hbar\omega)S_r(\varphi, \theta; \omega)$, where ω is the photon angular frequency, and $S_r(\varphi, \theta; \omega) = \frac{1}{2}\text{Re}\{\vec{E}(\varphi, \theta; r \rightarrow \infty) \times \vec{H}^*(\varphi, \theta; r \rightarrow \infty)\} \cdot \hat{r}$ is the time-averaged Poynting vector in the far field; \vec{E} and \vec{H} are the scattered electric and magnetic fields. Note that we use spherical coordinates here, to be consistent with the observed angle-resolved maps.

The reason behind observing the winding arms, instead of the donut-like intensities, is quantitatively explained as the interference between the generated LG waves and TR that is generated by the electron on impact (see [supplementary Figure S2](#)), similar to what was observed for interference between single plasmonic holes and TR.³³ The TR sustains a rather flat spectral feature so that this interference phenomenon, similar to the interference of LG waves with a reference Gaussian beam,³⁴ happens over a broad spectral range, as observed in [Figure 2](#).

[Figure 3](#) shows numerically simulated angle-resolved CL distributions of the Poynting vector at $\lambda = 495, 540$, and 651 nm. The winding arms are clearly resolved and cover a broad spectral range in agreement with the broadband data in [Figure 2](#). Comparing the calculated and measured CL distributions at $\lambda = 650$ nm, we find good agreement between the number of spiral arms and their handedness. At $\lambda = 650$ nm the calculated CL distributions closely follow the symmetry of the structure, whereas at shorter wavelengths, the results indicate more

complex angular distributions of the far-field light, which we attribute to the excitation of higher-order modes.

Field Dynamics. To gain a better understanding of the behavior of our structures upon electron impact and the mechanisms behind the generation of optical vortices, the dynamics of the electromagnetic fields in both time and frequency domains are closely explored. [Figure 4](#) shows the spatial distribution of the induced time-dependent E_z and H_z fields at selected times after the electron excitation and at two different heights, namely, 10 nm and $1 \mu\text{m}$ above the surface. Several generation, propagation, scattering, and radiation effects then lead to vortex light emission.

Radial SPP Generation. Upon the electron impact, a radially propagating SPP wavepacket is excited. By comparing time snapshots (data not shown), we find that SPPs propagate at a phase velocity close to the speed of light in vacuum, in agreement with the dispersion of the symmetric SPP mode (see [supplementary Figure S3](#)). The launched SPPs scatter off the holes in the chiral arms generating in-plane magnetic dipole moments in the holes. This is clearly seen in the magnetic near-field plots of [Figure 4a](#) ($z = 10$ nm), which shows intense magnetic field hot spots in the holes at all simulated times. At 6.72 fs (top left panel in [Figure 4a](#)) the SPPs (propagating at 300 nm/fs) have just reached the outer holes. At 11.34 and 14.81 fs the spiral still lights up brightly due to plasmon propagation along the hole spirals as well as reflection of SPPs from the outer ring. Note that larger holes at the end of the spiral show larger magnetic field intensities, which is due to the larger SPP scattering cross section and larger dipole moment. This wide hole size distribution results in broadband coupling of SPPs leading to the broadband emission of the vortex light seen in [Figure 2a](#). The electric field profiles in [Figure 4b](#) reflect the propagation of SPPs between the spirals ([supplemental movie S1](#)).

Magnetic Chain Plasmons. Strong far-field coupling between the excited hole plasmons leads to the formation of chain polaritons in which magnetic plasmons propagate along the hole array. Time movies of the field patterns ([supplemental movie S2](#)) clearly show the outward propagation of magnetic field components along the chain as time progresses. In contrast with planar SPPs, chain plasmons can show strong radiation loss

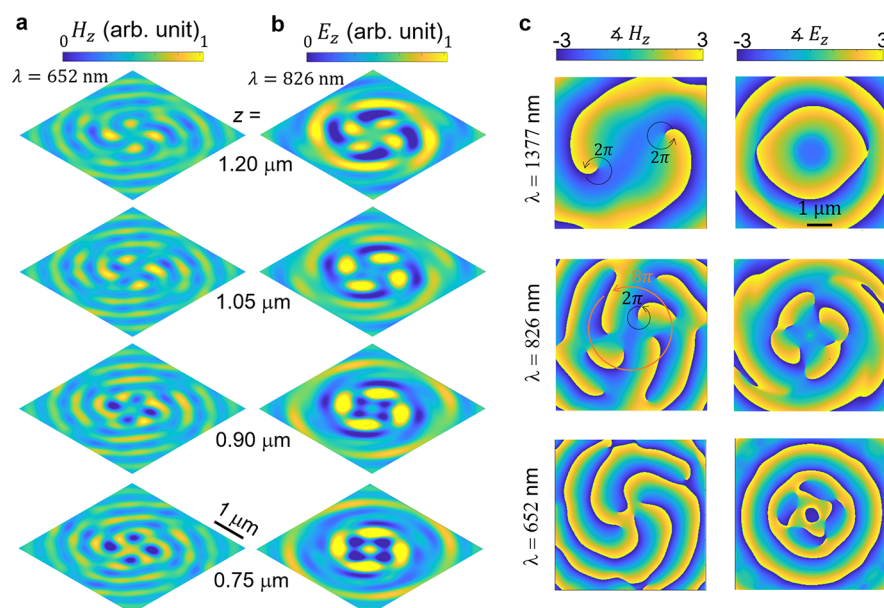


Figure 5. Fourier-transformed field components associated with TE_z and TM_z vortex light. *z*-components of (a) magnetic field ($\lambda = 652$ nm) and (b) electric field ($\lambda = 826$ nm), at distances in the range 0.75–1.20 μm from the structure, demonstrating the twisting behavior of optical fields with orbital angular momentum order of $l = 4$. (c) Phase profiles of optical modes sustained by the structure showing singularities akin to twisting vortices at the plane 1 μm above the structure. At $\lambda = 1377$ nm, only two phase singularity points are formed, and only TE_z modes with $l = +2$ are excited, whereas at higher photon energies, more phase singular regions leading to $l = +4$ for both TE_z and TM_z fields are observed.

at wavevectors within the light cone,^{31,35,36} thus contributing to the chiral radiation pattern. As the chain plasmon polaritons originate from magnetic dipole moments in nanoholes, they create TE-polarized LG wavepackets.

SPP Scattering and Propagation. Upon scattering off the holes, SPP will propagate along the chiral ribbons between the holes. These chirally scattered and propagating SPPs are TM-polarized, and all the field components can be calculated from the E_z component. The chiral SPPs flow pattern is the result of multiple scattering events from different holes, each generating magnetic hole plasmons that radiate to the far field as described above and generate TE-polarized waves.

Transition Radiation. Simultaneously to the initial generation of SPPs, TR is generated, as a result of the time-varying dipole associated with the moving electron and its image charge in the metal. This causes an ultrashort pulse of electromagnetic radiation covering a broad spectral range and angular distribution, as discussed above. The wavefront of TR is not changed by the presence of nanostructured holes. TR is characterized by the donut-shaped azimuthal distribution in the electric far-field pattern shortly after electron impact (10.05 fs). It expands further for later times (14.64 and 18.10 fs panels in Figure 4b).

The coherent superposition of all scattering processes described above leads to the vortex pattern observed in the far field. Both the magnetic and electric far-field patterns ($z = 1 \mu\text{m}$) in Figure 4a,b clearly reflect the vortex nature of the emitted radiation. After 10.07 fs, strong upward beaming of light appears in the far-field distributions, reflecting the time delay associated with the fact that plasmons first propagate in the plane and then scatter out. The spiral structure is now clearly imprinted on the scattered field. For the longer time delays [right-hand panels in Figure 4a,b] the far-field patterns strongly evolve further due to the interference between TR and scattered SPPs. Indeed, the angular orientation of the experimental angle-resolved CL data

directly matches the simulation and is the opposite of the spiral orientation on the sample.

So far, we have described the time-dependent field components obtained using FDTD calculations. To obtain insight into the spectral features and the phase singularities of the vortex beam, we study the frequency components of the radiated field. We therefore calculate the Fourier-transformed field components to obtain both the magnitude and phase of the field components at several wavelengths of a right-handed spiral with four arms at different heights (Figure 5a). The spirals retain their azimuthal orientation, in agreement with the time snapshots in Figure 4 and with what is observed experimentally.

We find that TE polarization dominates the LG waves at wavelengths $\lambda < 700$ nm, whereas at longer wavelengths, TM polarized LG waves are dominant (Figure 5a,b). This particularly indicates that the coupling strength between adjacent magnetic dipole moments excited inside nanoholes decreases when increasing the wavelength. Figure 5c demonstrates phase profiles of the vortex beams for the structure with 4 chiral arms at $\lambda = 652$, 826, and 1377 nm. As the centers of the arms are not perfectly located at the origin [which may be related to the discretization of the parameter t in eq 1], instead of observing a single phase-singularity in the center with $l = 4$ (as expected from a perfect LG mode in free space), four distinguished $l = 1$ points are observed. For the same reason, at longer wavelengths ($\lambda > 1200$ nm) we observe the excitation of an $l = 2$ mode as seen in the magnetic field. Therefore, depending on the path taken along a selected x – y plane, we might observe $\varphi = 0, 2\pi$, and 4π , at $\lambda = 1377$ nm, and $\delta\varphi = 0, 2\pi, 4\pi, 6\pi$, and 8π , at longer wavelengths (Figure 5c). Our observations thus hint at the possibility of expanding the generated waves as a superposition of LG waves with $p = 0$, and $l = 1$, where each beam is laterally displaced from the origin. Due to these variations, the generated vortex light does not have a perfect correspondence with a single LG Gaussian beam of a certain l -order, but only a similar distribution in the phase

pattern. Nevertheless, radial orders specified by a different p -parameter can be ruled out, as they would lead to radial variations in the observed CL pattern.

In summary, we have designed, fabricated, and characterized an electron-driven photon source based on a photon-sieve structure with a chiral distribution of nanoholes. The electrons create SPPs that scatter off the nanoholes and propagate along chiral nanoribbons between the arms. In addition, due to the interaction of propagating plasmons with the nanoholes, resonant magnetic dipole moments are induced in the nanoholes, which leads to the creation and propagation of chain magnetic plasmons along the chiral arms. This leads to the excitation of both TE- and TM-polarized LG waves over a broad spectral range. Interference between generated LG waves and transition radiation, generated by the same electron, encodes the phase of the LG waves into the detected intensity pattern, creating a clearly visible spiral pattern in the far field with angular momentum determined by the number of spirals. Combining our current analysis with our previous results on focused ultra-broadband radiation from a generic photon-sieve structure, we highlight the possibility of on-demand structuring of the cathodoluminescence light, which is favorable for conjugate electron–photon spectroscopy techniques with electron microscopes.

■ ASSOCIATED CONTENT

Supporting Information

The Supporting Information is available free of charge at <https://pubs.acs.org/doi/10.1021/acs.nanolett.0c01964>.

Movie of temporal rotation (MP4)

Time movies of the field patterns (MP4)

3D spatial distribution image, discussion of interference of Laguerre–Gauss beams with transition radiation, numerically calculated propagation constant with time snapshots of the magnetic field, methods (PDF)

■ AUTHOR INFORMATION

Corresponding Author

Nahid Talebi – Institute of Experimental and Applied Physics, Christian Albrechts University, 24118 Kiel, Germany;
✉ orcid.org/0000-0002-3861-1005; Email: talebi@physik.uni-kiel.de

Authors

Nika van Nielen – Center for Nanophotonics, AMOLF, 1098 XG Amsterdam, The Netherlands

Mario Hentschel – 4th Physics Institute and Research Center SCoPE, University of Stuttgart, 70550 Stuttgart, Germany

Nick Schilder – Center for Nanophotonics, AMOLF, 1098 XG Amsterdam, The Netherlands

Harald Giessen – 4th Physics Institute and Research Center SCoPE, University of Stuttgart, 70550 Stuttgart, Germany

Albert Polman – Center for Nanophotonics, AMOLF, 1098 XG Amsterdam, The Netherlands; ✉ orcid.org/0000-0002-0685-3886

Complete contact information is available at:

<https://pubs.acs.org/doi/10.1021/acs.nanolett.0c01964>

Author Contributions

N.T. conceived the idea and performed the simulations. M.H. fabricated the samples. N.v.N. performed the measurements. N.T. wrote the manuscript with contributions from all the

coauthors. All the coauthors actively contributed to the discussions and interpreting the results. H.G., A.P., and N.T. supervised the research.

Notes

The authors declare the following competing financial interest(s): A.P. is cofounder and co-owner of Delmic BV, a company that produces commercial cathodoluminescence systems like the one that was used in this work.

■ ACKNOWLEDGMENTS

This project has received funding from the European Research Council (ERC) under the European Union's Horizon 2020 research and innovation programme, grant agreements No. 802130 (Kiel, NanoBeam), 695343 (AMOLF, SCEON), and (Stuttgart, ComplexPlas). M.H. and H.G. acknowledge financial support from the Bundesministerium für Bildung und Forschung, Deutsche Forschungsgemeinschaft (SPP1839) and Baden-Württemberg Stiftung. Work at AMOLF is partly financed by the Dutch Research Council (NWO).

■ REFERENCES

- (1) García de Abajo, F. J. Optical excitations in electron microscopy. *Rev. Mod. Phys.* **2010**, *82* (1), 209–275.
- (2) Ginzburg, V. L. *Progress in Optics*; Elsevier: 1993; Vol. 32.
- (3) Ginzburg, V. L. Radiation from uniformly moving sources (Vavilov-Cherenkov effect, transition radiation, and some other phenomena). *Acoust. Phys.* **2005**, *51* (1), 11–23.
- (4) Wendin, G.; Nuroh, K. Bremsstrahlung Resonances and Appearance-Potential Spectroscopy near the \$3d\$ Thresholds in Metallic Ba, La, and Ce. *Phys. Rev. Lett.* **1977**, *39* (1), 48–51.
- (5) Ciarrocchi, E.; Belcari, N. Cerenkov luminescence imaging: physics principles and potential applications in biomedical sciences. *EJNMMI Phys.* **2017**, *4* (1), 14–14.
- (6) Polman, A.; Kociak, M.; García de Abajo, F. J. Electron-beam spectroscopy for nanophotonics. *Nat. Mater.* **2019**, *18* (11), 1158–1171.
- (7) Newbury, D. E.; Ritchie, N. W. M. Elemental mapping of microstructures by scanning electron microscopy-energy dispersive X-ray spectrometry (SEM-EDS): extraordinary advances with the silicon drift detector (SDD). *J. Anal. At. Spectrom.* **2013**, *28* (7), 973–988.
- (8) Smith, S. J.; Purcell, E. M. Visible Light from Localized Surface Charges Moving across a Grating. *Phys. Rev.* **1953**, *92* (4), 1069–1069.
- (9) Bratman, V. L.; Dumes, B. S.; Fedotov, A. E.; Makhalov, P. B.; Movshevich, B. Z.; Rusin, F. S. Terahertz Orotrons and Oromultipliers. *IEEE Trans. Plasma Sci.* **2010**, *38* (6), 1466–1471.
- (10) Adamo, G.; Ou, J. Y.; So, J. K.; Jenkins, S. D.; De Angelis, F.; MacDonald, K. F.; Di Fabrizio, E.; Ruostekoski, J.; Zheludev, N. I. Electron-Beam-Driven Collective-Mode Metamaterial Light Source. *Phys. Rev. Lett.* **2012**, *109* (21), 217401.
- (11) Li, G.; Clarke, B. P.; So, J.-K.; MacDonald, K. F.; Zheludev, N. I. Holographic free-electron light source. *Nat. Commun.* **2016**, *7* (1), 13705.
- (12) Talebi, N. Spectral Interferometry with Electron Microscopes. *Sci. Rep.* **2016**, *6* (1), 33874.
- (13) Talebi, N.; Meuret, S.; Guo, S.; Hentschel, M.; Polman, A.; Giessen, H.; van Aken, P. A. Merging transformation optics with electron-driven photon sources. *Nat. Commun.* **2019**, *10* (1), 599.
- (14) Allen, L.; Padgett, M. J.; Babiker, M. IV The Orbital Angular Momentum of Light. In *Progress in Optics*; Wolf, E., Ed.; Elsevier: 1999; Vol. 39, pp 291–372.
- (15) Ruffato, G.; Massari, M.; Romanato, F. Multiplication and division of the orbital angular momentum of light with diffractive transformation optics. *Light: Sci. Appl.* **2019**, *8* (1), 113.
- (16) Barnett, S. M.; Babiker, M.; Padgett, M. J. Optical orbital angular momentum. *Philos. Trans. R. Soc., A* **2017**, *375* (2087), 20150444.

- (17) Fernandez-Corbaton, I.; Fruhnert, M.; Rockstuhl, C. Objects of Maximum Electromagnetic Chirality. *Phys. Rev. X* **2016**, *6* (3), 031013.
- (18) Rubinsztein-Dunlop, H.; Forbes, A.; Berry, M. V.; Dennis, M. R.; Andrews, D. L.; Mansuripur, M.; Denz, C.; Alpmann, C.; Banzer, P.; Bauer, T.; Karimi, E.; Marrucci, L.; Padgett, M.; Ritsch-Marte, M.; Litchinitser, N. M.; Bigelow, N. P.; Rosales-Guzmán, C.; Belmonte, A.; Torres, J. P.; Neely, T. W.; Baker, M.; Gordon, R.; Stilgoe, A. B.; Romero, J.; White, A. G.; Fickler, R.; Willner, A. E.; Xie, G.; McMorran, B.; Weiner, A. M. Roadmap on structured light. *J. Opt.* **2017**, *19* (1), 013001.
- (19) Schattschneider, P. *Linear and Chiral Dichroism in the Electron Microscope*; Jenny Stanford Publishing: 2012.
- (20) Verbeeck, J.; Tian, H.; Schattschneider, P. Production and application of electron vortex beams. *Nature* **2010**, *467* (7313), 301–304.
- (21) Grillo, V.; Tavabi, A. H.; Venturi, F.; Larocque, H.; Balboni, R.; Gazzadi, G. C.; Frabboni, S.; Lu, P.-H.; Mafakheri, E.; Bouchard, F.; Dunin-Borkowski, R. E.; Boyd, R. W.; Lavery, M. P. J.; Padgett, M. J.; Karimi, E. Measuring the orbital angular momentum spectrum of an electron beam. *Nat. Commun.* **2017**, *8* (1), 15536.
- (22) Vanacore, G. M.; Berruto, G.; Madan, I.; Pomarico, E.; Biagioni, P.; Lamb, R. J.; McGrouther, D.; Reinhardt, O.; Kaminer, I.; Barwick, B.; Larocque, H.; Grillo, V.; Karimi, E.; García de Abajo, F. J.; Carbone, F. Ultrafast generation and control of an electron vortex beam via chiral plasmonic near fields. *Nat. Mater.* **2019**, *18* (6), 573–579.
- (23) Spektor, G.; Kilbane, D.; Mahro, A. K.; Frank, B.; Ristok, S.; Gal, L.; Kahl, P.; Podbiel, D.; Mathias, S.; Giessen, H.; Meyer zu Heringdorf, F.-J.; Orenstein, M.; Aeschlimann, M. Revealing the subfemtosecond dynamics of orbital angular momentum in nanoplasmonic vortices. *Science* **2017**, *355* (6330), 1187–1191.
- (24) Guo, Z.; Li, Z.; Zhang, J.; Guo, K.; Shen, F.; Zhou, Q.; Zhou, H. Review of the Functions of Archimedes' Spiral Metallic Nanostructures. *Nanomaterials* **2017**, *7* (11), 405.
- (25) Hachtel, J. A.; Cho, S.-Y.; Davidson, R. B.; Feldman, M. A.; Chisholm, M. F.; Haglund, R. F.; Idrobo, J. C.; Pantelides, S. T.; Lawrie, B. J. Spatially and spectrally resolved orbital angular momentum interactions in plasmonic vortex generators. *Light: Sci. Appl.* **2019**, *8* (1), 33.
- (26) Hentschel, M.; Weiss, T.; Bagheri, S.; Giessen, H. Babinet to the Half: Coupling of Solid and Inverse Plasmonic Structures. *Nano Lett.* **2013**, *13* (9), 4428–4433.
- (27) Ögüt, B.; Vogelgesang, R.; Sigle, W.; Talebi, N.; Koch, C. T.; van Aken, P. A. Hybridized Metal Slit Eigenmodes as an Illustration of Babinet's Principle. *ACS Nano* **2011**, *5* (8), 6701–6706.
- (28) Coenen, T.; Polman, A. Optical Properties of Single Plasmonic Holes Probed with Local Electron Beam Excitation. *ACS Nano* **2014**, *8* (7), 7350–7358.
- (29) Zentgraf, T.; Meyrath, T. P.; Seidel, A.; Kaiser, S.; Giessen, H.; Rockstuhl, C.; Lederer, F. Babinet's principle for optical frequency metamaterials and nanoantennas. *Phys. Rev. B: Condens. Matter Mater. Phys.* **2007**, *76* (3), 033407.
- (30) Maier, S. A.; Kik, P. G.; Atwater, H. A. Observation of coupled plasmon-polariton modes in Au nanoparticle chain waveguides of different lengths: Estimation of waveguide loss. *Appl. Phys. Lett.* **2002**, *81* (9), 1714–1716.
- (31) Raeis Zadeh Bajestani, S. M.; Shahabadi, M.; Talebi, N. Analysis of plasmon propagation along a chain of metal nanospheres using the generalized multipole technique. *J. Opt. Soc. Am. B* **2011**, *28* (4), 937–943.
- (32) Coenen, T.; Vesseur, E. J. R.; Polman, A.; Koenderink, A. F. Directional Emission from Plasmonic Yagi–Uda Antennas Probed by Angle-Resolved Cathodoluminescence Spectroscopy. *Nano Lett.* **2011**, *11* (9), 3779–3784.
- (33) Schilder, N.; Agrawal, H.; Garnett, E. C.; Polman, A. Phase-resolved surface plasmon scattering probed by cathodoluminescence holography. *ACS Photonics* **2020**, *7*, 1476–1482.
- (34) Weber, K.; Hütt, F.; Thiele, S.; Gissibl, T.; Herkommer, A.; Giessen, H. Single mode fiber based delivery of OAM light by 3D direct laser writing. *Opt. Express* **2017**, *25* (17), 19672–19679.
- (35) Maier, S. A.; Brongersma, M. L.; Kik, P. G.; Meltzer, S.; Requicha, A. A. G.; Atwater, H. A. Plasmonics—A Route to Nanoscale Optical Devices. *Adv. Mater.* **2001**, *13* (19), 1501–1505.
- (36) Koenderink, A. F.; de Waele, R.; Prangma, J. C.; Polman, A. Experimental evidence for large dynamic effects on the plasmon dispersion of subwavelength metal nanoparticle waveguides. *Phys. Rev. B: Condens. Matter Mater. Phys.* **2007**, *76* (20), 201403.